

Article

Presence of Induced Weak Ferromagnetism in Fe-Substituted $\text{YFe}_x\text{Cr}_{1-x}\text{O}_3$ Crystalline Compounds

Roberto Salazar-Rodriguez ^{1,*}, Domingo Aliaga Guerra ¹, Jean-Marc Greneche ², Keith M. Taddei ³, Noemi-Raquel Checca-Huaman ⁴, Edson C. Passamani ⁵ and Juan A. Ramos-Guivar ⁶

¹ Facultad de Ciencias, Universidad Nacional de Ingeniería (UNI), Av. Túpac Amaru 210, Rímac, Lima 15333, Peru

² Institut des Molécules and Matériaux du Mans (IMMM UMR CNRS 6283), University Le Mans, Avenue Olivier Messiaen, Cedex 9, 72085 Le Mans, France

³ Oak Ridge National Laboratory (ORNL), Oak Ridge, TN 37831, USA

⁴ Centro Brasileiro de Pesquisas Físicas (CBPF), R. Xavier Sigaud, 150, Urca, Rio de Janeiro 22290-180, Brazil

⁵ Departamento de Física, Universidade Federal do Espírito Santo, Vitória 29075-910, Brazil

⁶ Grupo de Investigación de Nanotecnología Aplicada para Biorremediación Ambiental, Energía, Biomedicina y Agricultura (NANOTECH), Facultad de Ciencias Físicas, Universidad Nacional Mayor de San Marcos, Av. Venezuela Cdra 34 S/N, Ciudad Universitaria, Lima 15081, Peru

* Correspondence: rsalazarr@uni.edu.pe; Tel.: +51-19-9161-9615

Abstract: Fe-substituted $\text{YFe}_x\text{Cr}_{1-x}\text{O}_3$ crystalline compounds show promising magnetic and multi-ferroic properties. Here we report the synthesis and characterization of several compositions from this series. Using the autocombustion route, various compositions ($x = 0.25, 0.50, 0.6, 0.75, 0.9$, and 1) were synthesized as high-quality crystalline powders. In order to obtain microscopic and atomic information about their structure and magnetism, characterization was performed using room temperature X-ray diffraction and energy dispersion analysis as well as temperature-dependent neutron diffraction, magnetometry, and ^{57}Fe Mössbauer spectrometry. Rietveld analysis of the diffraction data revealed a crystallite size of 84 (8) nm for YFeO_3 , while energy dispersion analysis indicated compositions close to the nominal compositions. The magnetic results suggested an enhancement of the weak ferromagnetism for the YFeO_3 phase due to two contributions. First, a high magnetocrystalline anisotropy was associated with the crystalline character that favored a unique high canting angle of the antiferromagnetic phase (13°), as indicated by the neutron diffraction analysis. This was also evidenced by the high magnetic hysteresis curves up to 90 kOe by a remarkable high critical coercivity value of 46.7 kOe at room temperature. Second, the Dzyaloshinskii–Moriya interactions between homogenous and heterogeneous magnetic pairs resulted from the inhomogeneous distribution of Fe^{3+} and Cr^{3+} ions, as indicated by ^{57}Fe Mössbauer studies. Together, these results point to new methods of controlling the magnetic properties of these materials.

Keywords: DM interaction; crystalline YFeO_3 ; magnetic properties; enhanced weak ferromagnetism; exchange interactions



Citation: Salazar-Rodriguez, R.; Aliaga Guerra, D.; Greneche, J.-M.; Taddei, K.M.; Checca-Huaman, N.-R.; Passamani, E.C.; Ramos-Guivar, J.A. Presence of Induced Weak Ferromagnetism in Fe-Substituted $\text{YFe}_x\text{Cr}_{1-x}\text{O}_3$ Crystalline Compounds. *Nanomaterials* **2022**, *12*, 3516. <https://doi.org/10.3390/nano12193516>

Academic Editors: Jordi Sort, Zhenxiang Cheng, Chang-hong Yang and Chunchang Wang

Received: 5 September 2022

Accepted: 29 September 2022

Published: 8 October 2022

Publisher's Note: MDPI stays neutral with regard to jurisdictional claims in published maps and institutional affiliations.



Copyright: © 2022 by the authors. Licensee MDPI, Basel, Switzerland. This article is an open access article distributed under the terms and conditions of the Creative Commons Attribution (CC BY) license (<https://creativecommons.org/licenses/by/4.0/>).

1. Introduction

Bulk orthoferrites and orthochromites have been the subject of various studies since the 1950s, but the interest of the scientific community has recently been renewed due to their possible technological applications in sensors, switching devices, and spintronics [1,2]. New research is focused on improving novel synthesis methods, consequently producing materials with different and improved magnetic and electrical properties. It is important first to point out that the first publications were carried out almost exclusively with single crystal samples, a synthesis process that requires specialized equipment not often found in ordinary laboratories, and that inherently prevents the production of large quantities of materials [3,4]. Currently, new synthesis methods have been explored to produce polycrystalline samples that have the advantage of rapid preparation, low cost, and the ability

to produce relatively large masses of material [4]. On the other hand, developments in nanotechnology have also made it possible to obtain nanocrystalline orthoferrites with highly controlled stoichiometry using wet methods, such as the sol–gel approach, allowing continuous doping between the orthoferrite and orthochromite endmembers [5]. Such synthesis developments may be instrumental in studying the Fe–Cr phase diagram, which has been historically challenging due to the thermodynamic considerations of the Y_2O_3 – Fe_2O_3 binary phase diagram, in which magnetite or ternary garnets can easily be obtained as parasitic (or secondary) phases. Therefore, the use of these new techniques to scale up the synthesis and carefully control the composition allows unprecedented access to the Fe–Cr phase diagram, potentially enabling the optimization and understanding of the interesting magnetic properties of these materials.

The $YFeO_3$ orthoferrite (YFO) and the $YCrO_3$ orthochromite (YCO) compounds crystallize in the $Pnma$ centrosymmetric space group symmetry and are biferroic with high Néel temperatures (T_N). Specifically, these materials are antiferromagnetic with $T_N = 644$ K and 140 K for YFO and YCO, respectively, with the a -direction of the unit cell as the easy magnetization axis. Moreover, these materials exhibit weak ferromagnetism, which has been attributed to the canting of magnetic moments along the c -direction, leading to the convincing observation of ferromagnetic behavior [5]. As early as the 1960s, Treves [6] proposed an antisymmetric interaction mechanism (Dzyaloshinskii–Moriya (DM) exchange) for this type of ferromagnetism in orthoferrites based on torque measurements in single crystals of rare earth orthoferrites ($RFeO_3$, $R =$ rare earth and Y). Considering these intriguing physical properties and the possibility to combine the two above materials (i.e., forming a Fe-substituted YCO phase), improved electrical and magnetic properties are expected. In particular, the case of the $YFe_{0.5}Cr_{0.5}O_3$ compound is very interesting because it has the largest magnetoelectric effect in the series [7] and may present a spin reorientation phenomenon according to the literature [8]. However, most of these studies have been performed on bulk polycrystalline samples, leaving the effects of another tuning parameter, namely, the crystallite size, unstudied. To optimize and understand the magnetoelectric effect in these materials, one could use the crystalline size as well as the application of large magnetic fields to try to stabilize different magnetic configurations or tune the canting angle and thus potentially improve the magnetoelectric effect.

In this work, the structural and magnetic properties of the Fe-substituted YCO phase (i.e., the $YFe_xCr_{1-x}O_3$ compounds) in the crystalline regime are studied in detail. The structural and composition features were obtained from Rietveld refinements and scanning electron microscopy (SEM), which showed (i) a single phase in the studied compounds and (ii) their nanoscale characteristics. The magnetic properties of the Fe-substituted compounds were studied by performing direct current magnetization measurements at and between 300 K (room temperature (RT)) and 5 K using both zero-field-cooling (ZFC) and field-cooling (FC) protocols, while the local magnetic properties were investigated using ^{57}Fe Mössbauer spectrometry performed at 300 K and 77 K and under an external magnetic field. The obtained results suggested an enhancement of WFM associated mainly with the sub-micrometric size character of the YFO phase (84 (8) nm), which has favored a relevant spin canting of 13° , i.e., a net spin contribution related to the sample finite-size effect. This property is not observed in the single and polycrystalline systems reported in the literature. In addition, the presence of the finite-size effect (spin-canting) in our sample was also reflected in the increase of the saturation magnetization that reached 0.79 emu/g at 3.5 kOe.

2. Materials and Methods

The whole series of $YFe_xCr_{1-x}O_3$ perovskites was synthesized by the combustion method by stoichiometrically mixing the following initial reactants: $Y(NO_3)_3 \cdot 6H_2O$, $Fe(NO_3)_3 \cdot 9H_2O$, $Cr(NO_3)_3 \cdot 9H_2O$, urea, and glycine. To improve the crystallization process, all powder samples were heated up to 1200 °C and annealed under ambient conditions. The synthe-

sized samples were labeled as the RSx series, where RS1, RS2, RS3, RS4, RS5, RS6, and RS7 correspond to $x = 0, 0.25, 0.50, 0.60, 0.75, 0.90,$ and $1.0,$ respectively.

Structural characterization was carried out using Bruker Advance D8 X-ray diffraction equipment (Bruker Corporation, Billerica, MA, USA), operating with a Cu-K α radiation source (1.5418 Å wavelength), and the X-ray diffraction (XRD) diffractograms were recorded at RT with a 2θ from 15° to 65° in a step of 0.02° and with an accumulating time of 10 s. Neutron diffraction (NPD) of the RS3 (YFe_{0.5}Cr_{0.5}O₃) sample was performed on the HB-2A line of the High Flux Isotope Reactor (HFIR) at Oak Ridge National Laboratory (ORNL) [9]. X-ray and NPD data were analyzed using the FullProf suite (Gif sur Yvette Cedex, France, version January 2021). In all nuclear diffraction peak modeling, the previously reported orthorhombic crystal structure (space group Pnma) was found to account for all observed peak positions and intensities, identified using the software Match v3. As initial cell parameter values, we employed $a = 5.59$ Å, $b = 7.59$ Å, and $c = 5.27$ Å (Match entry 210–1387) and allowed the parameters to refine during the profile fitting for the different temperatures and compositions. The instrumental resolution function (IRF) of the X-ray diffractometer was obtained from the aluminum oxide (Al₂O₃) standard with Caglioti parameters: $U = 0.0093,$ $V = -0.0051,$ and $W = 0.0013$ [10]. The morphology, size, and composition of the powders were obtained using a TESCAN LYRA3 high-resolution scanning electron microscope (Tescan Brno s.r.o., Brno, Czech Republic) with an FEG type electron source coupled with an Oxford energy-dispersive X-ray spectroscopy (EDS) detector. Secondary electron imaging and atomic element mapping were acquired simultaneously using an accelerating voltage of 15 kV and a working distance of 9 mm.

Zero-field-cooling (ZFC) magnetic hysteresis loops ($M(H)$ loops) were recorded at 300 K and 5 K using the vibrating sample magnetometer (VSM) option operating in a Dynacool (Quantum Design North America, San Diego, CA, USA) setup for a maximum applied field of 90 kOe. ZFC and warm-field-cooling (WFC) magnetization measurements, $M(T),$ were performed under two different probe fields: 50 Oe and 1000 Oe.

⁵⁷Fe Mössbauer spectra were obtained with WissEl equipment (WissEl—Wissenschaftliche Elektronik GmbH, Starnberg, Germany) in a transmission geometry using a ⁵⁷Co source diffused into an Rh matrix with an activity of about 1.5 GBq and mounted on a conventional constant acceleration vibrating electromagnetic transducer. The sample was in the form of a powder layer containing about 5 mg Fe/cm². Spectra were obtained at 300 K and at 77 K in a bath cryostat. A thin foil of α -Fe was used at 300 K for calibration of the spectrometry (isomer shift values are given relative to Fe at 300 K). The modeling of the hyperfine structures was performed using a homemade Mosfit program based on the least squares method, and magnetic and quadrupolar components were composed of Lorentzian peaks.

3. Results and Discussion

3.1. XRD and Rietveld Analysis

From the Rietveld refinement of the XRD and neutron diffraction powder (NPD) patterns measured at RT and 2 K, respectively, the results suggested for all samples the presence of only an orthorhombic Pnma (No. 62) crystal structure [11], i.e., no secondary phase was observed. In addition, both experiments showed similar behavior for the lattice parameters $a,$ $b,$ and c within their uncertainties. Thus, the refined values of the cell parameters are plotted in Figure 1a,b, which suggested: (i) a linear evolution of the cell parameters (Figure 1a) at RT and 2 K as a function of iron concentration (x), (ii) the c parameter changed more rapidly than the a or b parameters, and (iii) a continuous increase in cell volume with Fe concentration (Figure 1b) at both temperatures. For the size estimation of YFeO₃ crystallites (RS7 sample) (see refined diffractogram in Figure 1c), we used the modified Scherrer's formula that expresses the anisotropic size broadening as a linear combination of spherical harmonics (SHP) if the anisotropic size contribution

belongs only to the Lorentzian component of the total Voigt function [10]. Therefore, the explicit formula for the SPH approach of size broadening is given by Equation (1) [12]:

$$\beta_h = \frac{\lambda}{D_h \cos \theta} = \frac{\lambda}{\cos \theta} \sum_{lmp} a_{lmp} y_{lmp}(\Theta_h, \Phi_h) \quad (1)$$

where h is assigned to the (hkl) indices, β_h is the size contribution to the integral width of reflection (hkl), $y_{lmp}(\Theta_h, \Phi_h)$ are the real components of spherical harmonics (arguments Θ_h and Φ_h are the polar and azimuthal angles of vector (hkl) with respect to a Cartesian crystallographic frame), and a_{lmp} are the refined coefficients, related to the Laue class [13]. For the RS7 sample, a -1 Laue class was used.

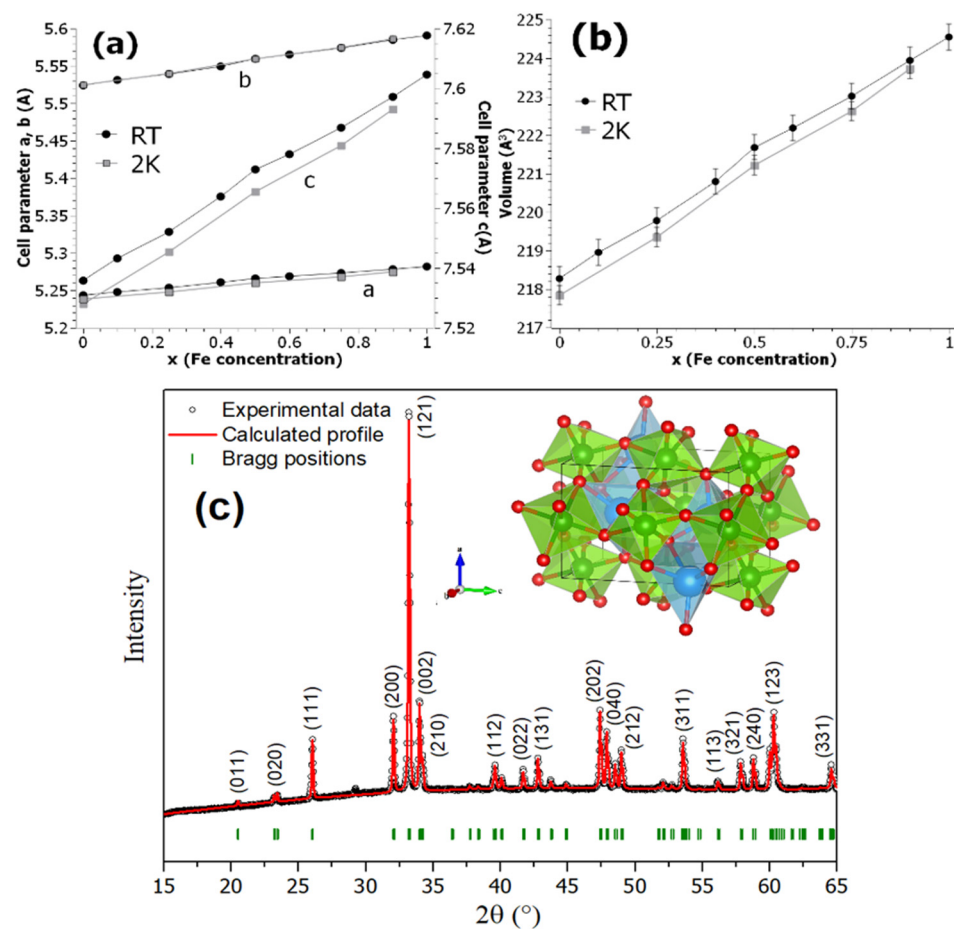


Figure 1. Cell parameter (a) and volume (b) variation with the x (Fe concentration) and Rietveld refinement XRD diffraction pattern (c) for the RS7 sample. The inset in (c) is the simulated structure obtained after refinement using VESTA (red spheres are oxygen atoms, white and blue are yttrium atoms, and green spheres are iron atoms). While blue, red, and green arrows indicate the a , b , and c crystallographic axes, respectively. Miller indexes are given between parentheses, black dots are the experimental data, the red line is the calculated diffraction pattern, and the vertical green lines are the Bragg's diffraction position. Solid lines in (a,b) are guides for visualization.

The obtained profile refinement gave acceptable statistical parameters for the reliability factor, R_p (%); weighted profile residual, R_{wp} (%); expected profile residual, R_{exp} (%); and goodness of fit, χ^2 ; having quantitative values as follows: $R_p = 16.2\%$, $R_{wp} = 10.4\%$, $R_{exp} = 26.19\%$, and $\chi^2 = 0.94$, while the refined harmonic coefficients were found equal to $Y_{00} = -0.00574$, $Y_{20} = 0.01395$, $Y_{21}^+ = -0.06448$, $Y_{21}^- = 0.01518$, $Y_{22}^+ = 0.07557$, and $Y_{22}^- = -0.03690$, respectively. With these values, the anisotropic Lorentzian size broadening gave a mean crystallite value of 84 (8) nm. Hence, combining all above data, it can be

inferred that the autocombustion method allowed nanocrystalline Fe-substituted YCrO_3 powders with a single phase, orthorhombic-like structure to be obtained.

3.2. SEM Analysis

For all samples, the autocombustion method with final annealing up to $1200\text{ }^\circ\text{C}$ yielded a distribution of agglomerates about ($\sim 200\text{--}500\text{ nm}$) that form a series of interconnected chains, as typical found in autocombustion synthesis [4]. In Figure 2a–q, the RSx series shows similar morphologies as those obtained by Zhang et al. [4,14]. In all of them, the notorious polycrystalline nature can be observed. The STEM images and elemental analyses given by yellow, red, blue, and green colors (Figure 2d–m) show the evolution of the systems when the Fe concentration increases. The systematic formation of the Fe-substituted YCrO_3 phase is noted in the EDS pattern given in Figure 2r, and the atomic percentage contribution is summarized in Table 1. We can roughly say that the particles produced by this combustion method have a similar morphology and similar dispersion in all tested concentrations. In addition, considering the uncertainties of the element contents in the samples, we can also affirm that Y and O are quite constant, while Fe increases and Cr decreases its contribution; this indicates that Fe enters the crystalline cell, due to the larger ionic radius of Fe^{3+} (0.645 \AA) (compared to $\text{Cr}^{3+} = 0.615\text{ \AA}$), which is consistent with the unit cell volume determined from X-ray and neutron diffractions, as previously discussed.

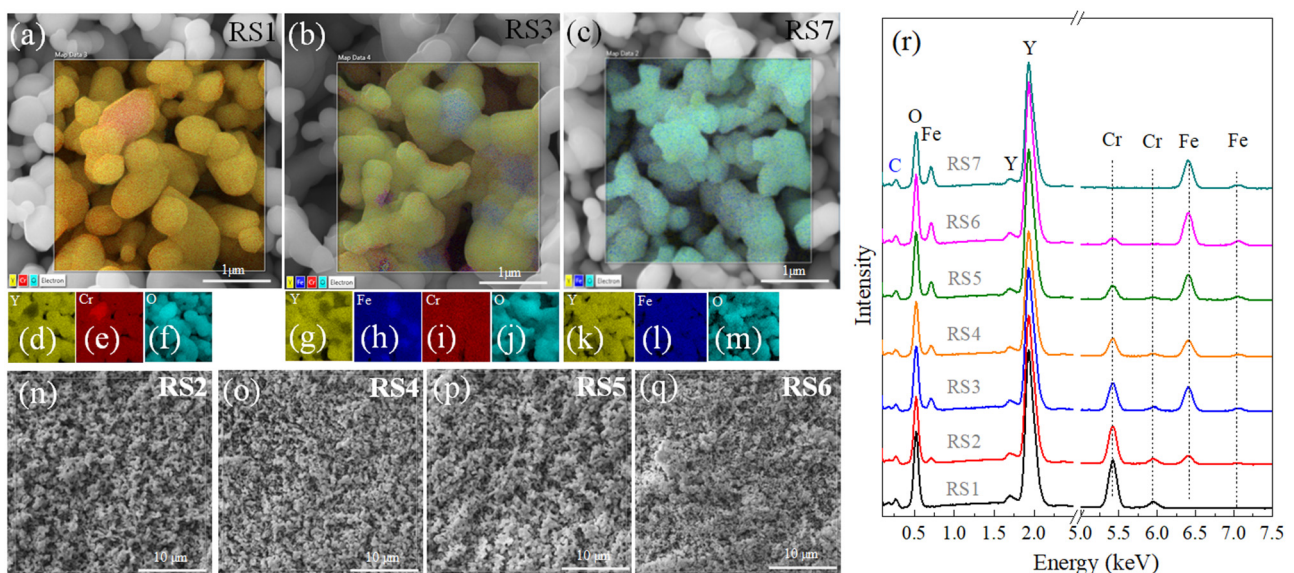


Figure 2. (a–c) SEM images for the RS1, RS3, and RS7 samples (bar length = $1\text{ }\mu\text{m}$). The magnified area was performed in high resolution mode, and the elemental mapping area for each sample is given in (d–m) images. SEM images for the RS2, RS4, RS5, and RS6 samples (n–q) (bar length = $10\text{ }\mu\text{m}$). (r) The EDS for the RS1–RS7 samples.

Table 1. Weight percentage composition of the elements found in all samples.

Sample	Y (% wt) ± 2	Cr (% wt) ± 2	Fe (% wt) ± 1	O (% wt) ± 1
RS1	52	31	-	17
RS2	51	25	9	15
RS3	47	17	23	14
RS4	51	14	20	15
RS5	51	9	25	16
RS6	51	4	30	15
RS7	51	-	33	16

3.3. VSM Analysis

Figures 3 and 4 illustrate the ZFC ± 90 kOe $M(H)$ curves of the $\text{YFe}_x\text{Cr}_{1-x}\text{O}_3$ series taken at 5 K (top) and 300 K (bottom), respectively. At RT, the samples with $x = 0.25$ and 0.50 behaved as ordinary paramagnets (see Figure 3d,f), while the samples with $x = 0.60, 0.75,$ and 0.90 suggested an onset of a weak ferromagnetism (see Figure 4b,d,f). For the $x = 1.0$ sample (YFeO_3 compound, RS7), shown in Figure 5a, $M(H)$, curves recorded at different temperatures show the magnetic features of a weak ferromagnet with high magnetic anisotropy, i.e., with characteristics similar to that found in the pure YFeO_3 compound (set-like $M(H)$ curve). Therefore, this sample (RS7) revealed an interesting and complex magnetic behavior that is mainly attributed in the literature to an exchange spring effect. In particular, the magnetic spring effect can be often observed by an exchange magnetic coupling between coexisting and interacting soft and hard magnets in a sample, as reported by Popkov et al. [5].

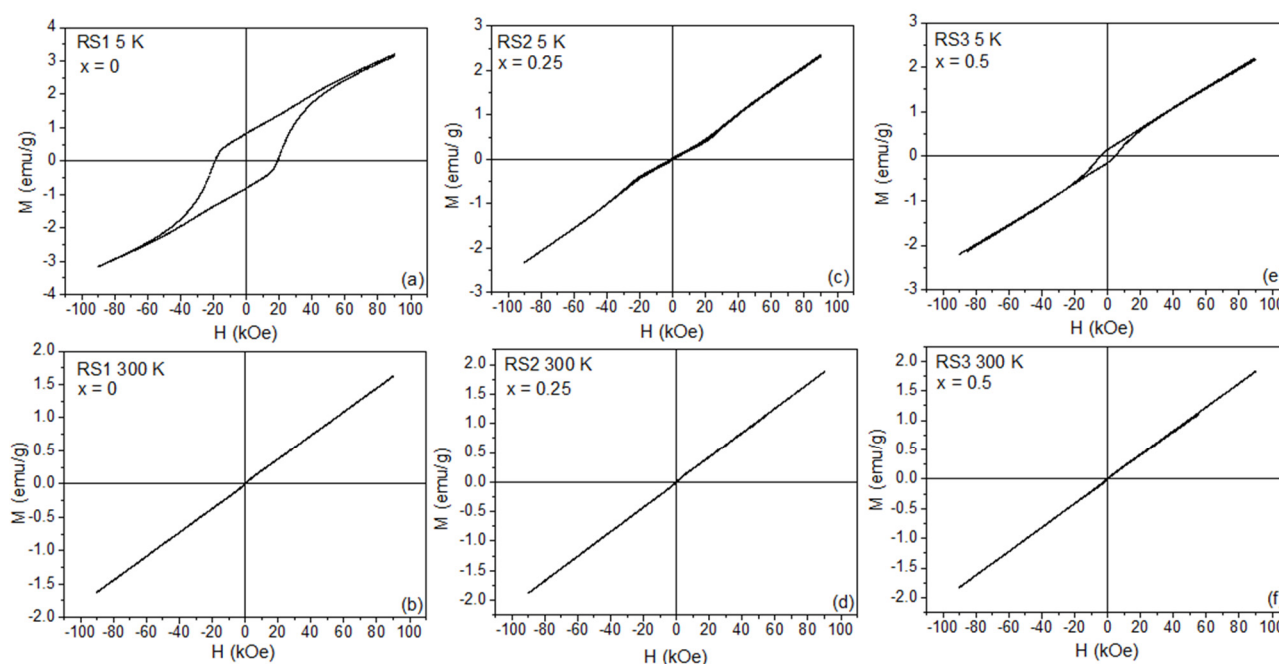


Figure 3. $M(H)$ curves recorded for a maximum field of 90 kOe at 5 K (top) and 300 K (bottom) for the RSX samples. RS1 in (a,b), RS2 in (c,d), and RS3 in (e,f), respectively.

Thus, since the NDP, Rietveld, and SEM data of the SR7 sample suggested the presence of a single-phase structure, and the presence of two magnetic phases of two crystalline structures (as occurs in bilayer films) cannot be inferred as a reason for the observed phenomenon. However, the atomic disordering in the orthorhombic structure and the change in cell volume could lead to local different magnetic phases, which will be magnetically interacting and producing the observed $M(H)$ behavior discussed above.

Looking at the 5 K $M(H)$ loop for the $x = 0$ sample (see Figure 3a), we can observe the characteristic $M(H)$ curve reported for the YCrO_3 compound [15]. Below T_N , the non-saturation regime of the $M(H)$ curve occurred till values of +90 kOe, indicating a remarkable antiferromagnetic state, while above T_N , a paramagnetic-like behavior was regarded; see Figure 3b. On the other hand, the loss of hysteresis in the RS2 and RS6 samples (Figure 3c,e and Figure 4a,c,e) indicated the substitution of Cr by Fe atoms in the orthorhombic crystal configuration, as confirmed by our XRD data. Table 2 contains the remanence (M_r), coercivity (H_C), and saturation magnetization (σ_{sat}) values of the hysteresis ferromagnetic part. Using the slope of the $M(H)$ curves, it was possible to subtract the antiferromagnetic contribution of the $M(H)$ curves, thus leaving the purely ferromagnetic component, as shown in Figure 5b. Thus, these $M(H)$ curves recorded at

different temperatures really showed large H_C fields, but their value decreased when the temperature decreased, concomitantly with the increase of the saturation magnetization (the area inside the $M(H)$ loop remained nearly constant). In addition, all $M(H)$ curves show more clearly the step-like behavior near the zero-applied field region of the $M(H)$ curve, a feature discussed above and attributed to a magnetic spring-like effect.

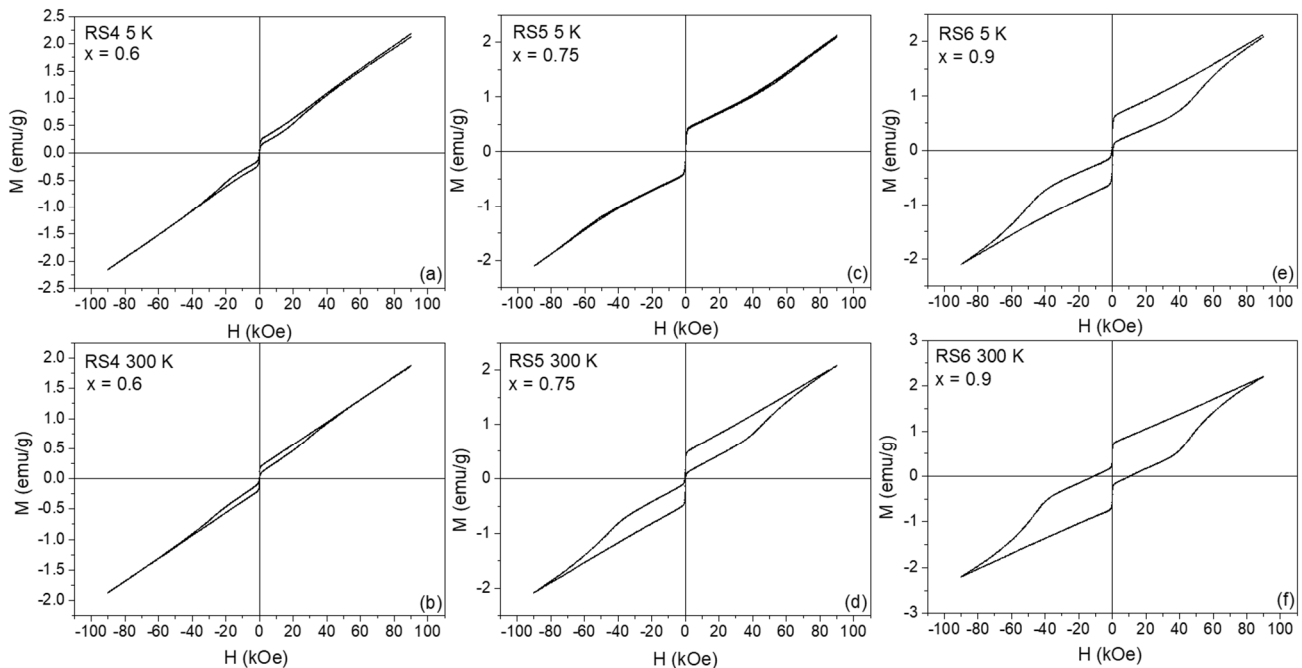


Figure 4. $M(H)$ curves recorded for a maximum field of 90 kOe at 5 (top) and 300 K (bottom) for the RSX samples. RS4 in (a,b), RS5 in (c,d), and RS6 in (e,f), respectively.

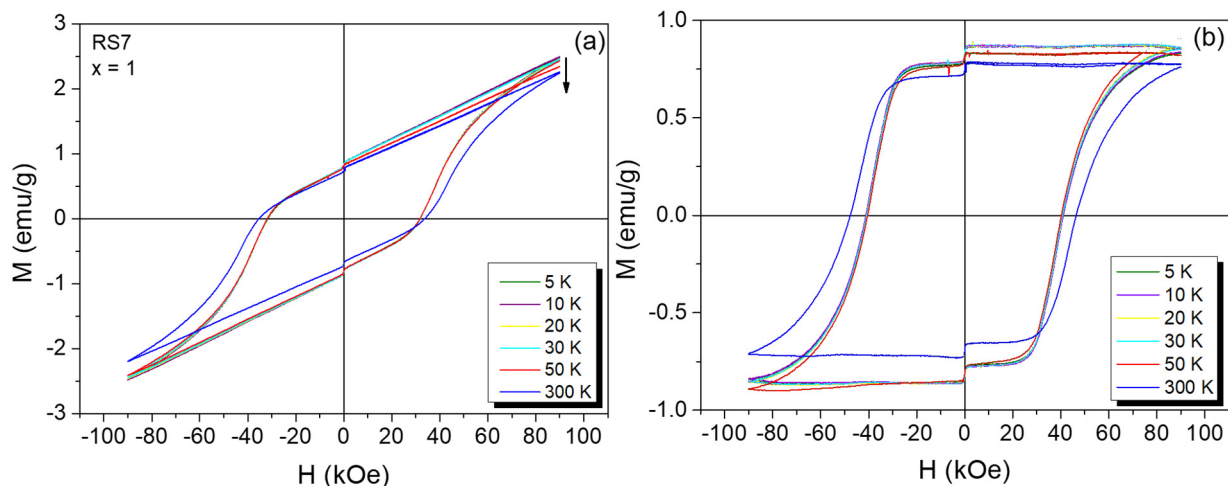


Figure 5. $M(H)$ loops for the RS7 sample recorded at different temperatures (a). $M(H)$ loops after the subtraction of the paramagnetic contribution of the AFM phase (b).

The magnetic parameters in Table 2 were plotted as a function of Fe concentration (x), as seen in Figure 6a,b,d. At 300 K, the H_C field dependence with x had two marked regions (I and II): (i) region-I can be interpreted as the magnetic domain reorientations (magnetization reversal) due to the increasing concentration of Fe atoms that are replacing Cr, forming the pure YFeO_3 crystalline phase; (ii) region-II has relatively high values of the H_C fields and that occur above $x = 0.75$, reaching a maximum value of 46.7 kOe for $x = 1$ (RS7 sample).

Table 2. Remanence (M_r), coercive field (H_C), and magnetic saturation (σ_{Sat}) of the ferromagnetic component, and susceptibility of the antiferromagnetic component to the RSx samples with $x = 1, 0.9, 0.75,$ and 0.60 . For the samples with $x = 0, 0.25,$ and 0.50 , the values correspond to the ‘paramagnetic’ state.

x	T (K)	M_r (emu/g) \pm 0.05	H_C (kOe) \pm 0.5	σ_{Sat} (emu/g) \pm 0.05	Susc. (emu/g \times Oe) \pm 0.01
1.00	300	0.75	46.7	0.79	0.02
1.00	5	0.84	40.9	0.87	0.02
0.90	300	0.64	43.2	0.77	0.02
0.90	5	0.27	0.3	0.61	0.02
0.75	300	0.18	0.3	0.55	0.02
0.75	5	0.02	0.02 (5)	0.41	0.02
0.60	300	0.05	0.1	0.20	0.02
0.60	5	0.05	0.1	0.23	0.02
0.50	300	0	0	0	0.02
0.50	5	0	0	0	0.02
0.25	300	0	0	0	0.02
0.25	5	0	0	0	0.03
0.00	300	0	0	0	0.02
0.00	5	0.80	18.9	0.89	0.03

The remanence (M_r) is calculated from $M_r = (M_{R+} + M_{R-})/2$, where M_{R+} and M_{R-} are the values of the upper and lower magnetization, respectively, when the magnetic field is zero. The coercive field (H_C) is calculated from $H_C = (H_{C+} - H_{C-})/2$, where H_{C+} and H_{C-} are the values of the right and left fields when magnetization is zero.

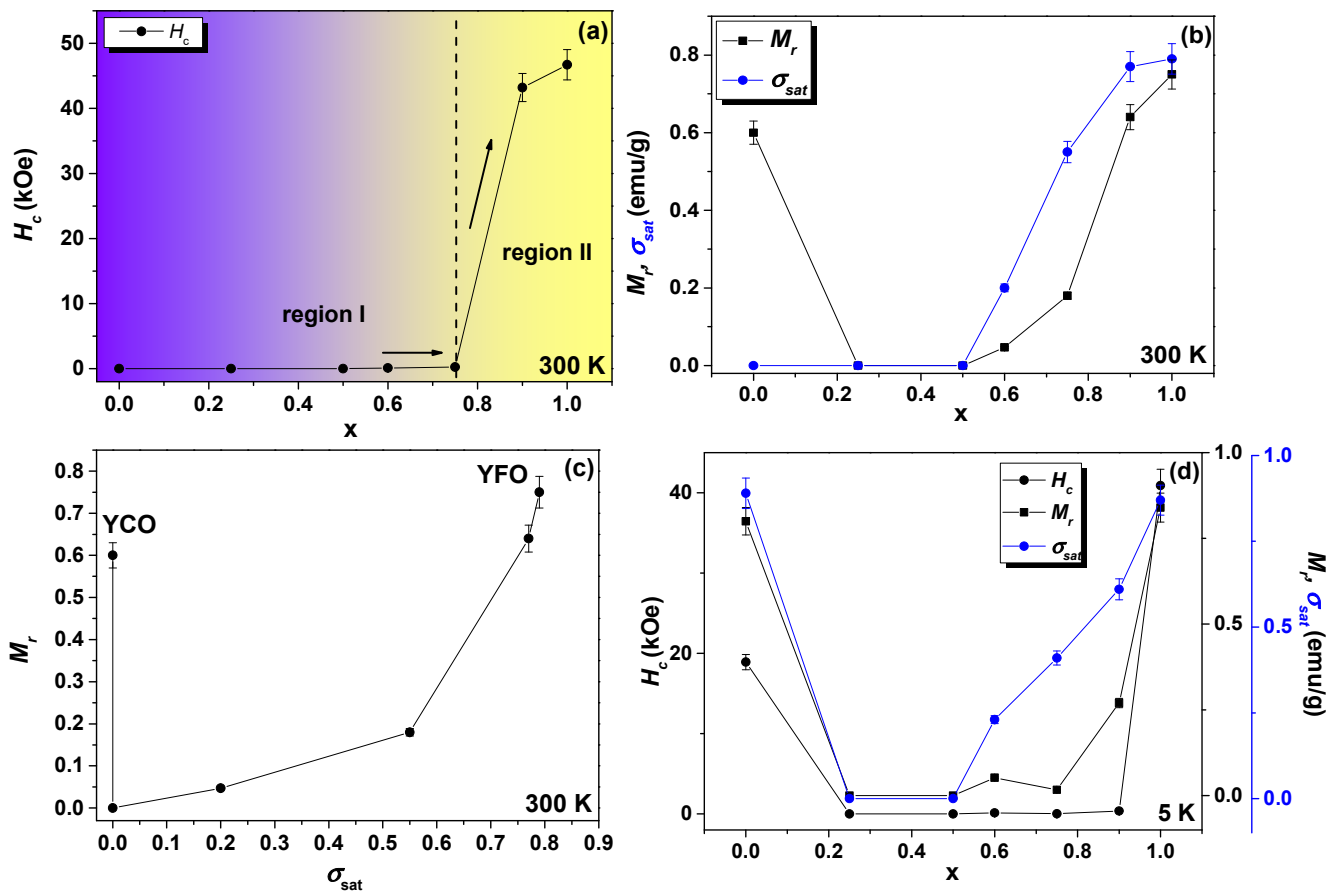


Figure 6. (a) Dependence of the H_C (kOe) vs. x (Fe concentration) at 300 K. (b) Dependence of the M_r and σ_{sat} vs. x (Fe concentration) at 300 K. (c) M_r vs. σ_{sat} graph at 300 K. (d) H_C , M_r , and σ_{sat} vs. x (Fe concentration) at 5 K.

These values were larger than those reported by Popkov et al. [5] for four YFeO₃ crystalline samples synthesized by different routes. On the other hand, the M_r and σ_{sat} values had a similar dependence with Fe concentration at 300 K and 5 K, as can be seen in Figure 6b,d. The behavior of M_r vs. σ_{sat} is shown in Figure 6c. The M_r and σ_{sat} quantities could reach maximum values of 0.75 and 0.79 emu/g, respectively. This σ_{sat} value of 0.79 emu/g was consistent with others found in the literature for either powder or single crystals [3,4,16–19], as summarized in Figure 7. In particular, the value of 0.79 emu/g, obtained for a field of 3.5 kOe, was almost two times higher than the values reported by Zhang et al. [4] and four times higher than that obtained by Shen et al. [20] for a similar system. Therefore, the RS7 sample behaved as an ordinary single crystal of the YFO phase with a multidomain magnetic structure [4,20]. In addition, it is worth mentioning that the RS7 sample exhibited weak ferromagnetism enhanced at 90 kOe.

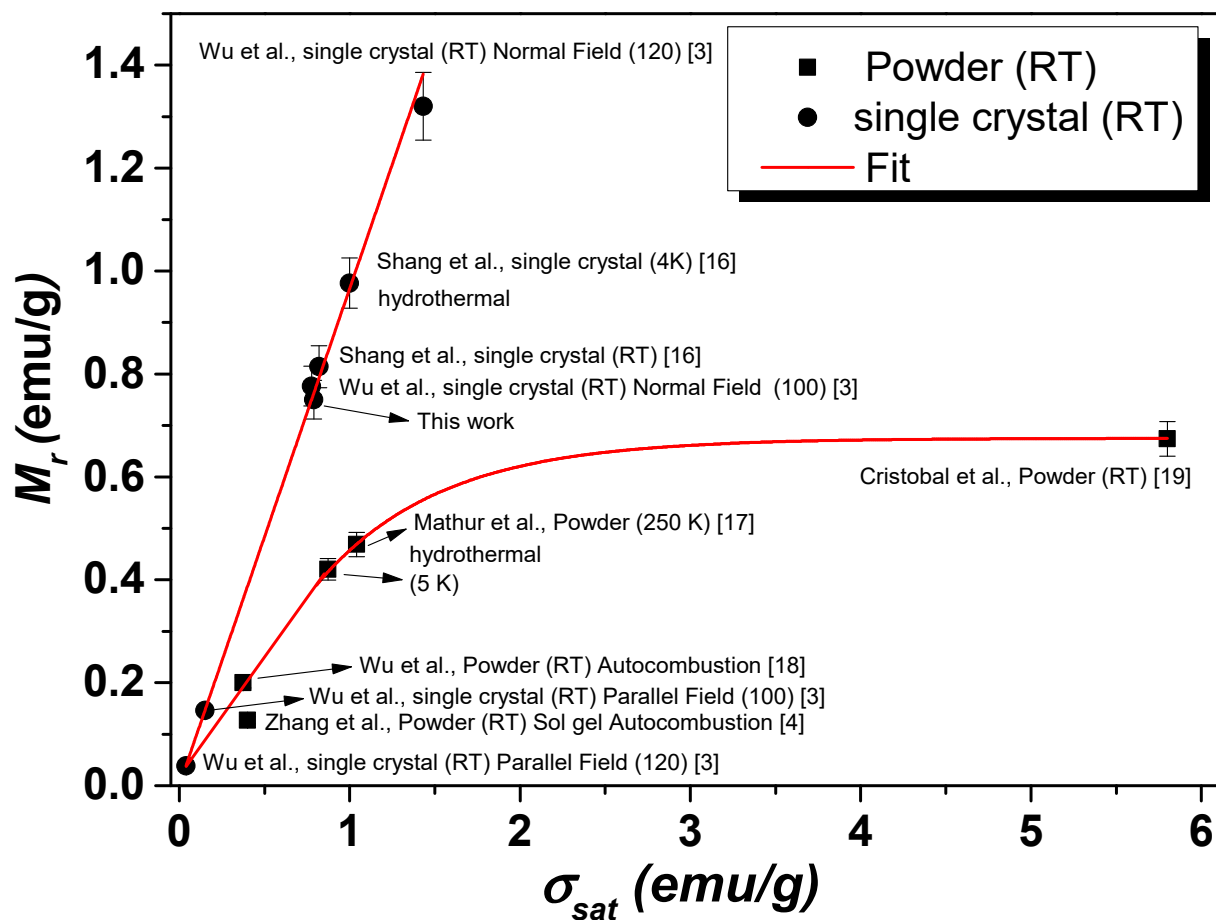


Figure 7. M_r vs. σ_{sat} relation built from data recorded at RT and reported in the literature for similar compounds. Comparison between powder and single crystal YFe_xCr_{1-x}O₃ [3,5,16–19].

The WFC and ZFC $M(T)$ measurements for all RSx samples were collected under two probe fields, namely, 50 Oe and 1000 Oe, and the results are shown in Figures 8–10. For the lowest applied field, the ZFC and WFC $M(T)$ curves, displayed in Figure 8a, clearly show the magnetization transition from the AFM to PM state of the YCrO₃ compound at 159 K, assigned to T_N . No other magnetic transition was observed in $M(T)$ curves, indicating that no secondary phase was formed during the auto combustion synthesis, in agreement with the XRD data. For the YFe_{0.25}Cr_{0.75}O₃ compound, the T_N value increased to 174 K (see Figure 8b), but a further increase of Fe content, for example, $x = 0.50$, led to a cancellation of total magnetization and a compensation temperature between the antiferromagnetic sub-lattices of 245 K. The zero-net magnetization was observed as an enhancement of the

diamagnetism contribution, as shown in Figure 8c. At $x = 0.60$ and 0.75 , see Figure 8d,e, a slight increase in the magnetization was observed, in agreement with the onset of WFM, as also seen in the $M(H)$ curves. At $x = 0.90$ and 1.0 (Figures 8f and 9), a significant increase in the magnetization was observed with significant overlap between ZFC and WFC $M(T)$ curves above 250 K.

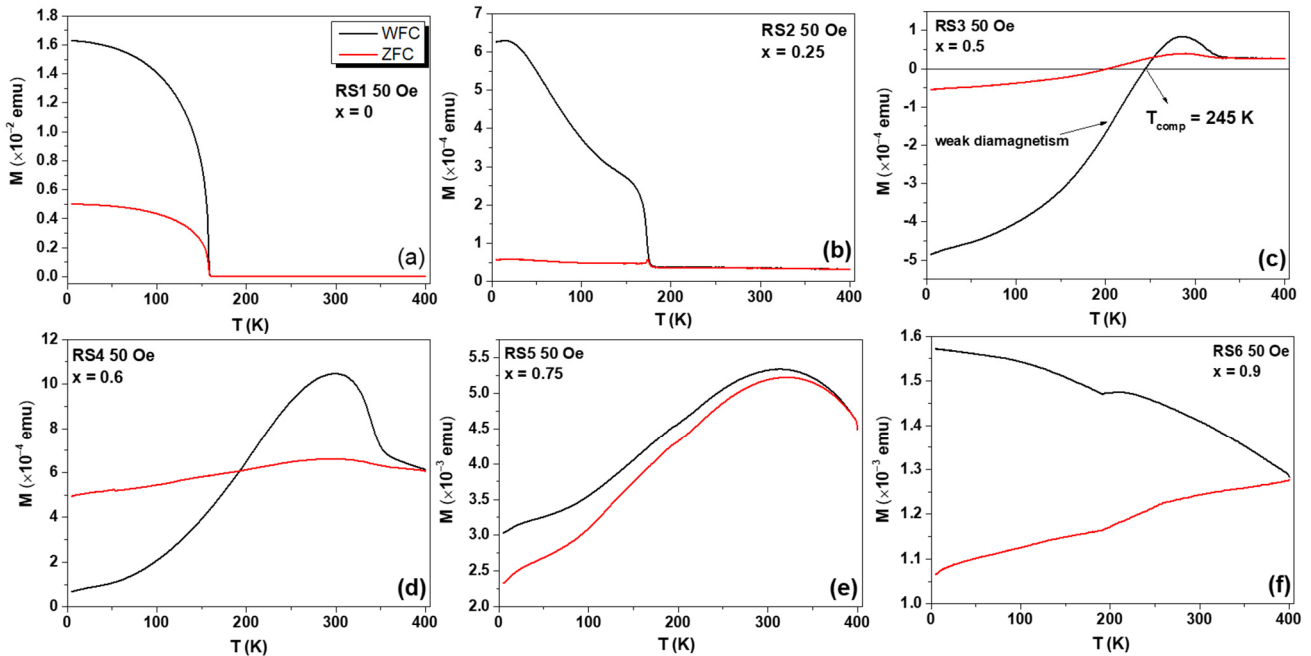


Figure 8. ZFC and WFC $M(T)$ curves at a probe field of 50 Oe for the (a) RS1, (b) RS2, (c) RS3, (d) RS4, (e) RS5, and (f) RS6 samples.

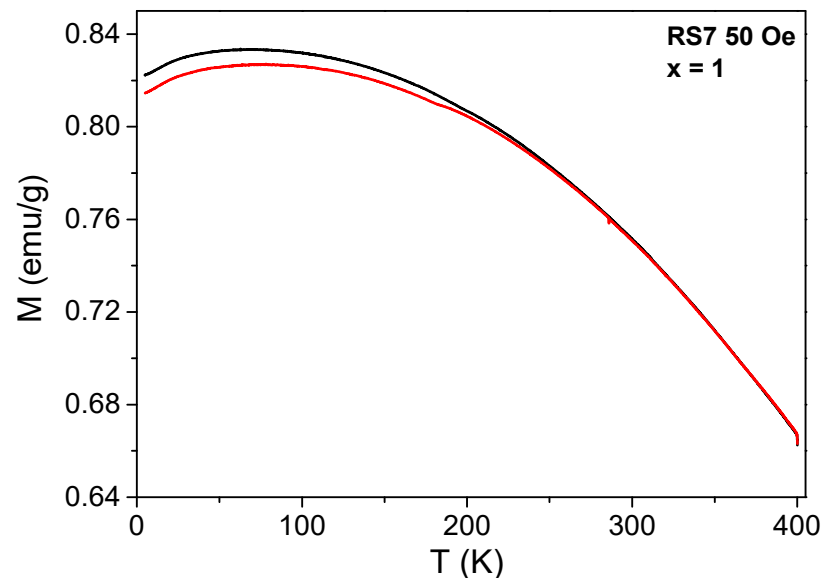


Figure 9. ZFC and WFC $M(T)$ curves recorded for a probe field of 50 Oe for the RS7 sample. Black line indicates WFC and red line ZFC, respectively.

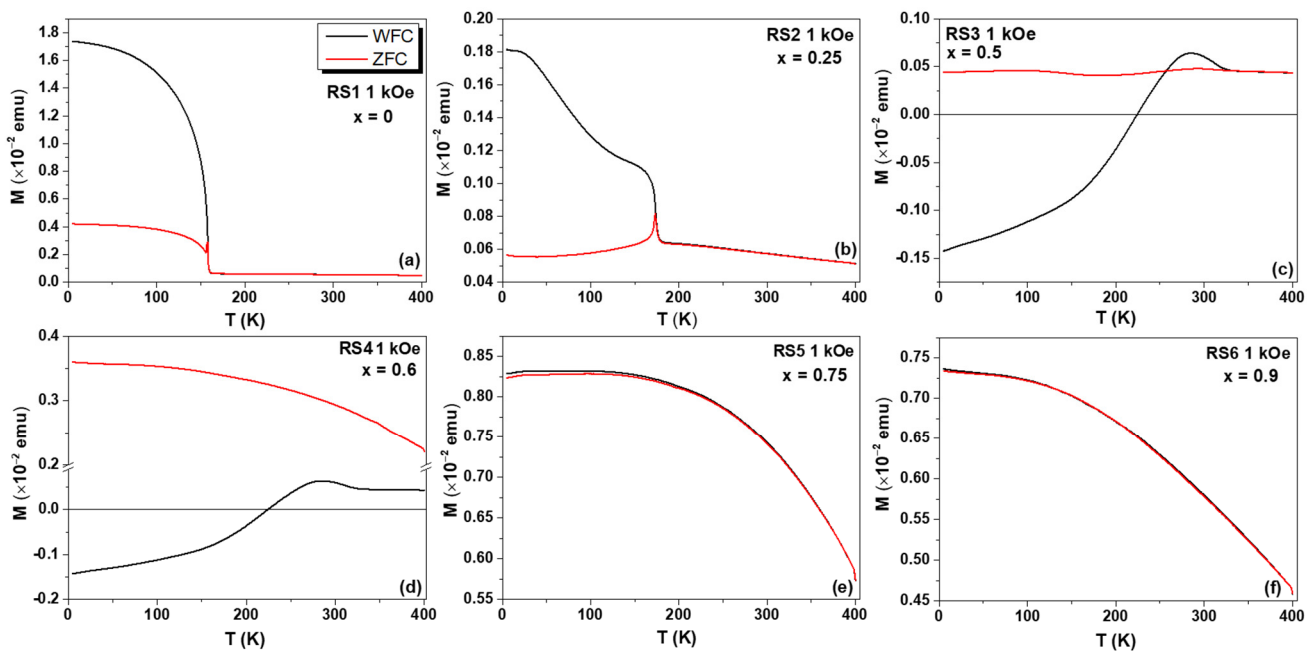


Figure 10. ZFC and WFC $M(T)$ curves recorded at a probe field of 1000 Oe for the (a) RS1, (b) RS2, (c) RS3, (d) RS4, (e) RS5, and (f) RS6 samples.

The determination of the T_N of the Fe-substituted YCO compounds was done recording the ZFC and WFC $M(T)$ curves at a higher field (1000 Oe). At this probe field, the magnetization of the samples with $x = 0.75$ and $x = 0.90$ showed a strong interaction with the external field, confirming the enhancement of the WFM. From ca. 5 K to higher temperatures, both ZFC and WFC $M(T)$ curves coincided for the sample with $x = 0.9$.

Based on the above experimental results, it can be inferred that the anisotropic exchange-spring in crystalline compounds cause a significant increase in the coercive field of 46.7 kOe at 300 K. This interesting magnetic response has also been observed by Popkov et al. [5]. In our case, the hard and soft magnetic phases are intrinsically correlated to the same structure, but they are due to chemical disorders in the sites of the orthorhombic crystal nanostructure. Moreover, the hysteresis loop shape depends on the finite-size effects under an applied DC magnetic field (in our case, we use the highest value reported in the literature of 90 kOe). Hence, the observed ascending/descending hysteresis loops at several temperatures is explained due to spin reorientation of the antiferromagnetic vector in the x - z plane, reaching the z -axis at a critical magnetic field, as reported by Jacobs et al. [21], where a value of 74 kOe at 4.2 K was obtained for the YFeO_3 single crystal. According to Popkov et al. [5], in nanocrystalline materials, the typical WFM hysteresis cycle is observed only for the YFO phase when their grain sizes are equal and larger than 41 nm, i.e., the YFO material may exhibit WFM, and the exchange spring-like effect may occur due to its high magnetocrystalline anisotropy energy. Consequently, considering our experimental results that showed a grain size of 84 (8) nm, we can also expect the observed ascending/descending branch behaviors of the $M(H)$ loops of the YFO sample. More precisely, the combined magnetic effects of the enhanced WFM and the presence of AFM interactions among the Fe ions of the different sites of the orthorhombic crystal structure gave rise to different local anisotropy contributions, producing high magnetocrystalline anisotropy due to the size effect and the enhancement of DM (Dzyaloshinskii–Moriya) interactions in the samples.

The two effects cannot be separated, and the improvement of WFM features can be explained assuming a canting angle of 13° , as demonstrated by previous neutron diffraction analysis [11]. The presence of AFM interactions in the Fe-substituted YCO compounds is also confirmed by the changes of T_N values as a function of Fe content, as displayed in Figure 11. Indeed, the T_N values increase nonlinearly with increasing Fe content, reaching

the reference value for YFO [8]. Of course, the Fe substitution phenomenon is randomly changing locally the anisotropy by changing the lattice parameters, as shown by the XRD results. These modifications favor the spin reorientation and magnetization reversal phenomena.

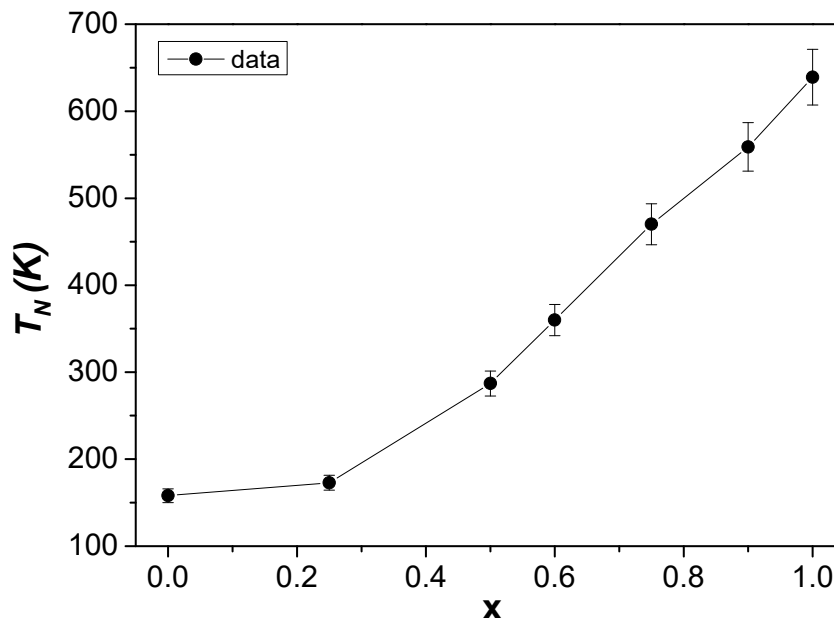


Figure 11. Néel temperature T_N dependence on x (Fe concentration) estimated from 1000 Oe $M(T)$ curves. The solid line passing by experimental points is only a guide for viewing.

3.4. Mössbauer Analysis

3.4.1. Measurements at 300 K

In agreement with the magnetization data, the 300 K ^{57}Fe Mössbauer spectra recorded for samples with different Fe concentrations show, on the one hand, partial ($x = 0.50$) or total ($x = 0.25$) paramagnetic behavior (see Figure 12a). On the other hand, the 300 K ^{57}Fe Mössbauer spectra of the samples with $x = 0.75$ and 1.0 show six absorption lines due to the nuclear Zeeman interaction with a local magnetic hyperfine field (B_{hf}). The refined values of the corresponding hyperfine parameters are given in Table 3. The values of isomer shift are typical of the presence of Fe^{3+} ions. Another important feature that should be highlighted is that the line widths of the Mössbauer spectra are generally broader for samples with $x = 0.25$, 0.50, and 0.75 compared with those of the RS7 sample ($x = 1.0$), the latter being expected to show less atomic disorder. Therefore, the broadening effect of magnetic lines is probably caused by different iron environments, since in the orthorhombic crystal structure of these perovskites, a $3d^5 \text{Fe}^{3+}$ ion is usually surrounded by 2, 3, 4, 5, or 6 Cr^{3+} ions in octahedral sites. The result of the chemical disorder is a hyperfine magnetic field distribution, i.e., a distribution of static sextets. In particular, the fit of the ^{57}Fe Mössbauer spectrum of the sample with $x = 0.50$ was done with two magnetic sextets and one quadrupolar doublet. The two sextets will represent the different local Fe environments of the orthorhombic crystal structure, while the doublet, best seen in the inset spectrum recorded in a low-velocity range, must be associated with Fe^{3+} ions in the paramagnetic state resulting from Cr^{3+} -rich environments ($T_N < 300$ K, e.g., for the $x = 0.25$, $T_N = 153$ K). The features discussed above tell us that the Fe substitution is not homogeneous, leading to an assembly of clusters with different compositions, i.e., a chemical disorder in the octahedral sites (B-sites) of the orthorhombic crystal structure. Thus, the largest magnetic component can be attributed to Fe^{3+} ions preferentially surrounded by Fe^{3+} ions ($T_N > 300$ K), while the quadrupolar doublet is associated with a neighborhood rich in Cr^{3+} ions, of course, with T_N values lower than 300 K, as shown by our magnetization data.

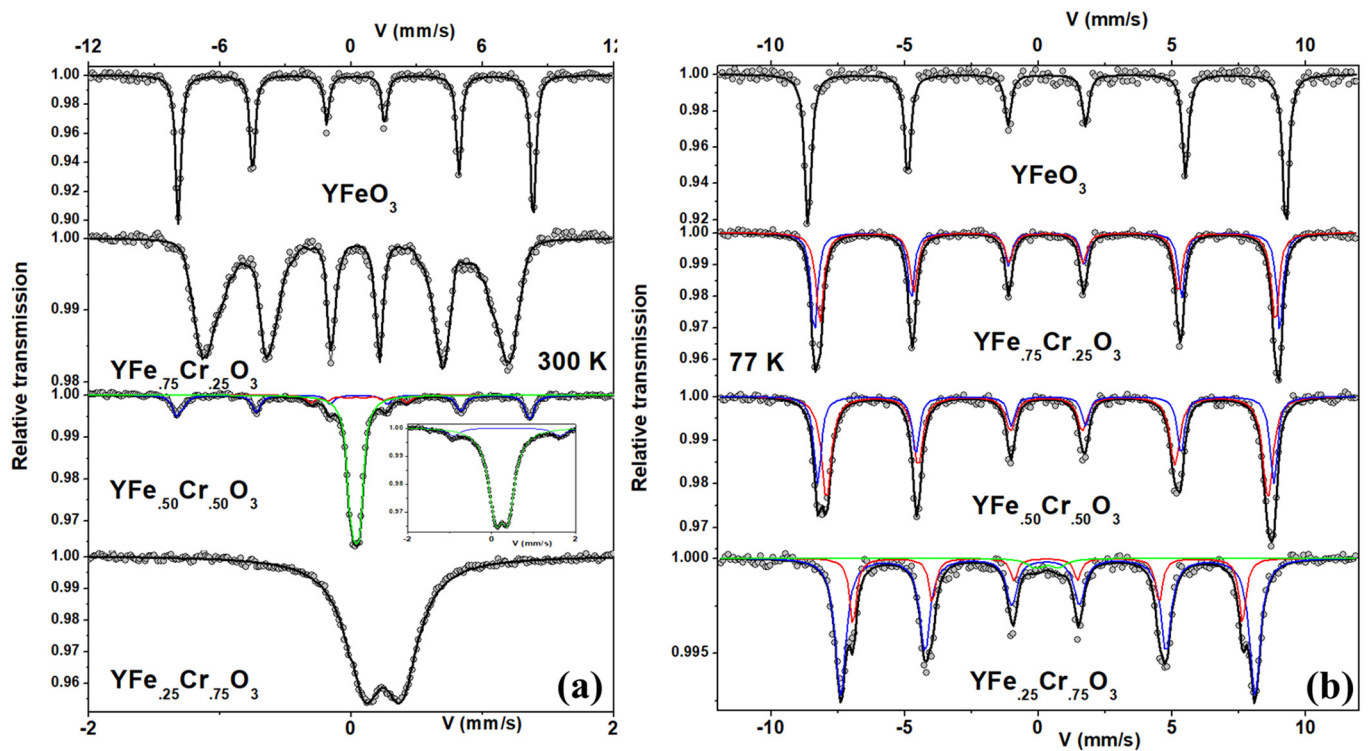


Figure 12. (a) RT Mössbauer measurements of the Fe-substituted $\text{YFe}_x\text{Cr}_{1-x}\text{O}_3$ compounds. Samples with $x = 1.0, 0.75,$ and 0.5 are measured with ± 12 mm/s. The inset shows the same spectra for $x = 0.5$ but with a maximal velocity of ± 2 mm/s, as in the case of the $\text{YFe}_{0.25}\text{Cr}_{0.75}\text{O}_3$ sample (last spectrum). (b) Same sample measured at 77 K. The subspectra used to fit these spectra are also shown. The two sextets represent the two iron configurations in octahedral sites of the orthorhombic crystal structure of the perovskite.

Table 3. Refined values of the hyperfine parameters at given temperatures.

x	T (K)	IS (mm/s) ± 0.01	2ε or Δ (mm/s) ± 0.01	B_{hf} (T) ± 0.5	Absorption Area Ratio % ± 2
1	300	0.37	0.00	50.1	100
	77	0.48	0.01	55.2	100
0.75	300	<0.38>	<0.04>	<40.7>	100
	77	0.47	0.03	53.8	49
		0.47	0.05	52.6	51
		<0.47>	<0.04>	<53.2>	
0.50	300	0.39	0.28		62
		0.40	−0.24	50.1	22
		0.46	−0.12	48.5	8
		0.35	0.15	13.3	8
	77	0.48	0.02	51.0	62
	0.48	−0.10	52.7	38	
		<0.48>	<−0.02>	<51.7>	
0.25	300	0.36	0.28		100
	77	0.47	0.08	47.9	74
		0.47	0.08	45.0	23
		0.47	0.79		3

3.4.2. Measurements at 77 K

To better understand the local environment of the ^{57}Fe ions in the orthorhombic crystal structure, additional measurements were made at 77 K for all Fe-substituted series, and the corresponding Mössbauer spectra are shown in Figure 12b. At 77 K, below the T_N values of the Fe-substituted YCO compounds (see Figure 11), one would therefore expect a pure Zeeman nuclear interaction in all ^{57}Fe spectra. The spectra, in general, show all six expected absorption lines, but with different broadening and asymmetries depending on the Fe content. While the 77 K Mössbauer spectrum of the YFO ($x = 1$) compound can be perfectly described by a single magnetic component, those of RS5, RS3, and RS2 require at least two magnetic components. The refined values of the hyperfine parameters are given in Table 3. Thus, to fit these 77 K spectra, we have two magnetic sextets to account for, at least, two octahedral configurations of Fe^{3+} ions for samples with non-zero x . The results clearly show that B_{hf} values decrease with increasing content. Even at 77 K, the spectrum of the $\text{YFe}_{0.25}\text{Cr}_{0.75}\text{O}_3$ sample required an additional quadrupolar doublet, with a fraction of 5% of total spectra. Thus, considering that the magnetization data show a T_N value for this sample equal to 153 K, the quadrupolar doublet must be associated with Fe^{3+} ions with a Cr^{3+} ion-rich neighborhood.

According to the Néel temperature of the series, it is understandable why the samples with $x = 1.0$ and 0.75 show hysteresis cycles, although the YFeO_3 sample has a lower magnetic energy than the 50% sample. Similarly, for the other two samples with $x = 0.25$ and zero, the magnetic susceptibility is consistent with paramagnetic behavior, which is understandable due to their lower T_N values than 300 K. The series contains samples with weak ferromagnetism and paramagnetic behaviors.

In brief, 77 K Mössbauer spectra were fitted, at least, with two different octahedral environments for Fe ions, and the results suggest that the presence of Cr ions decreases the B_{hf} value, but the difference between the two sextets of the Fe-substituted YCO compounds increases, except for the pure YFO, where only the sextet was required to have a good fit of the spectrum. One explanation for this decrease may be due to competing mechanisms between the antiferromagnetic interactions between Fe–Fe, Fe–Cr, and Cr–Cr exchanges and the DM interaction. Indeed, the asymmetric DM interaction is known to be the main interaction responsible for the WFM observed in YFO, where the antiferromagnetic coupling mechanism is due to superexchange interactions between the t_{3g} – O – t_{3g} and e_g – O – e_g orbitals, whereas for the YCO compound, the mechanism is a coupling to the t – e orbitals [22–24]. Therefore, we have in the Fe-substituted YCO samples a mixed exchange mechanism that is enhanced by the atomic disorder naturally present in our samples. It can be expected that due to the Fermi contact and the transferred magnetic field contribution to the total hyperfine magnetic field depend on the s electrons and the superposition of $3d$, s , and p electrons, respectively, there is increasing competition of Fe environments as the iron concentration of the sample increases. An appropriate calculation using the mean field theory gave the relationship $J_{\text{Fe-Fe}} > J_{\text{Fe-Cr}} > J_{\text{Cr-Cr}}$ [8].

4. Conclusions

In the present work, the structural and magnetic properties of the Fe-substituted perovskite series were studied in detail. Specifically, the average crystalline grain size of the YFeO_3 compound, calculated using the harmonic spherical approach in a Rietveld refinement, was 84 (8) nm, a size where weak ferromagnetism can occur in this compound. In the Fe-substituted $\text{YFe}_x\text{Cr}_{1-x}\text{O}_3$ compounds, X-ray and neutron diffraction patterns collected at RT and 2 K gave a linear increase in the lattice parameters of the orthorhombic structure with increasing Fe concentration, where the c -parameter had the most pronounced increase. This increase obviously translates into an increase in the volume cell and consequently a change in the magnetocrystalline anisotropy of the samples, i.e., a magnetic anisotropy that depends on the Fe concentration. Considering that X-ray and neutron diffraction showed only one crystalline phase for all samples, and the above results of lattice parameters that showed a gradual increase with increasing iron content, we can highlight that autocom-

bustion is a useful method for the synthesis of pure YFeO_3 with high stoichiometry. The 90 kOe $M(H)$ curves taken at RT and 5 K for all Fe-substituted samples suggest the presence of spin reorientation and magnetization reversal phenomena associated with homogenous (Fe–Fe, Cr–Cr) and non-homogeneous pairs of 3d-ions (Fe–Cr). The dependence of the H_C , M_r , and σ_{sat} with Fe concentration clearly showed the onset of WFM for $x = 0.60$ – 0.80 values. For $x = 1.0$, the high H_C value of 46.7 kOe was calculated after subtracting the AFM contribution (linear contribution of the paramagnetic phase). This latter result implies that an enhancement in the WFM is achieved due to chemical inhomogeneity of the YFeO_3 phase. Moreover, the values of M_r and σ_{sat} at 300 K are in agreement with the values commonly found in single crystals. The WFC and ZFC $M(T)$ curves recorded at low (50 Oe) and high (1000 Oe) probe field analysis allowed the magnetic properties and global magnetic response of the spin reorientation process to be tuned. The high field $M(T)$ curves allowed for accurate determination of T_N values and showed a nonlinear dependence of T_N on Fe concentration. The sample with $x = 0.75$ clearly exhibited a higher magnetic disorder, as corroborated by Mössbauer spectra recorded at 77 K and 300 K. The magnetization measurement performed in a low probe field of 50 Oe, for the sample with $x = 0.50$ showed a diamagnetic-like behavior near the compensation temperature of 245 K, where an inverse magnetization and the most intense remanence and saturation values at 300 K were found compared to the other samples. For the low Fe content ($x = 0.25$) and pure orthochromite samples, they showed paramagnetic-like behavior at RT, with a magnetic order only below 150 K. Mössbauer spectra allowed us to study the local Fe environment and visualize a weak enhanced ferromagnetism, due to a remarkable high canting angle (13°), estimated previously from neutron diffraction analysis, and its variation with Fe concentration. At least two octahedral Fe sites were identified in the non-pure Fe-substituted samples, whose evolution of the magnetic hyperfine field (B_{hf}) can be explained using the results of mean field theory reported in the literature. The sample with $x = 0.50$ showed good magnetic properties and is a suitable candidate for further study.

Author Contributions: Conceptualization, R.S.-R. and J.A.R.-G.; methodology, R.S.-R., N.-R.C.-H. and J.A.R.-G.; validation, R.S.-R., N.-R.C.-H., E.C.P., J.-M.G. and J.A.R.-G.; formal analysis, R.S.-R., N.-R.C.-H. and J.A.R.-G.; investigation, R.S.-R., D.A.G., K.M.T., N.-R.C.-H., E.C.P., J.-M.G. and J.A.R.-G.; resources, R.S.-R., N.-R.C.-H. and J.A.R.-G.; data curation, R.S.-R., N.-R.C.-H. and J.A.R.-G.; writing—original draft preparation, R.S.-R. and J.A.R.-G.; writing—review and editing, R.S.-R., E.C.P. and J.A.R.-G.; visualization, R.S.-R. and J.A.R.-G.; supervision, R.S.-R. and J.A.R.-G.; project administration, R.S.-R.; funding acquisition, R.S.-R. All authors have read and agreed to the published version of the manuscript.

Funding: This research was funded by the “Universidad Nacional de Ingeniería-UNI” and the APC was funded by VRI-UNI. The part of this research conducted at ORNL’s High Flux Isotope Reactor was sponsored by the Scientific User Facilities Division, Office of Basic Energy Sciences, US Department of Energy.

Data Availability Statement: The original data related to this research can be requested at any time from the corresponding author at the following email address: rsalazarr@uni.edu.pe.

Acknowledgments: We thank LABICER (UNI) for the XRD support and sample preparation analyzes. Juan A. Ramos-Guivar thanks the National Program of Scientific Investigation and Advanced Studies (PROCIENCIA), while Edson C. Passamani thanks FAPES and CNPq for their financial support.

Conflicts of Interest: The authors declare no conflict of interest.

References

1. Neusser, S.; Grundler, D. Magnonics: Spin Waves on the Nanoscale. *Adv. Mater.* **2009**, *21*, 2927–2932. [[CrossRef](#)]
2. Song, C.; You, Y.; Chen, X.; Zhou, X.; Wang, Y.; Pan, F. How to Manipulate Magnetic States of Antiferromagnets. *Nanotechnology* **2018**, *29*, 112001. [[CrossRef](#)]
3. Wu, A.; Shen, H.; Xu, J.; Wang, Z.; Jiang, L.; Luo, L.; Yuan, S.; Cao, S.; Zhang, H. Crystal Growth and Magnetic Property of YFeO_3 crystal. *Bull. Mater. Sci.* **2012**, *35*, 259–263. [[CrossRef](#)]

4. Zhang, W.; Fang, C.; Yin, W.; Zeng, Y. One-Step Synthesis of Yttrium Orthoferrite Nanocrystals Via Sol-Gel Auto-Combustion and Their Structural and Magnetic Characteristics. *Mater. Chem. Phys.* **2013**, *137*, 877–883. [[CrossRef](#)]
5. Popkov, V.I.; Almjashaeva, O.V.; Semenova, A.S.; Kellerman, D.G.; Nevedomskiy, V.N.; Gusarov, V.V. Magnetic Properties of YFeO₃ Nanocrystals Obtained by Different Soft-Chemical Methods. *J. Mater. Sci. Mater. Electron.* **2017**, *28*, 7163–7170. [[CrossRef](#)]
6. Treves, D. Magnetic Studies of Some Orthoferrites. *Phys. Rev.* **1962**, *25*, 1843–1853. [[CrossRef](#)]
7. Mao, J.; Sui, Y.; Zhang, X.; Su, Y.; Wang, X.; Liu, Z.; Wang, Y.; Zhu, R.; Wang, Y.; Liu, W.; et al. Temperature- and Magnetic-Field-Induced Magnetization Reversal in Perovskite YFe_{0.5}Cr_{0.5}O₃. *Appl. Phys. Lett.* **2011**, *98*, 192510. [[CrossRef](#)]
8. Dasari, N.; Mandal, P.; Sundaresan, A.; Vidhyadhiraja, N.S. Weak Ferromagnetism and Magnetization Reversal in YFe_{1-x}Cr_xO₃. *EPL* **2012**, *99*, 17008. [[CrossRef](#)]
9. Calder, S.; An, K.; Boehler, R.; Dela Cruz, C.R.; Frontzek, M.D.; Guthrie, M.; Haberl, B.; Huq, A.; Kimber, S.A.J.; Liu, J.; et al. A Suite-Level Review of the Neutron Powder Diffraction Instruments at Oak Ridge National Laboratory. *Rev. Sci. Instrum.* **2018**, *89*, 092701. [[CrossRef](#)] [[PubMed](#)]
10. Canchanya-Huaman, Y.; Mayta-Armas, A.F.; Pomalaya-Velasco, J.; Bendezú-Roca, Y.; Guerra, J.A.; Ramos-Guivar, J.A. Strain and Grain Size Determination of CeO₂ and TiO₂ Nanoparticles: Comparing Integral Breadth Methods versus Rietveld, μ -Raman, and TEM. *Nanomaterials* **2021**, *11*, 2311. [[CrossRef](#)]
11. Salazar-Rodriguez, R.; Aliaga-Guerra, D.B.; Taddei, K.M. X-Ray Diffraction, Mössbauer Spectroscopy, Neutron Diffraction, Optical Absorption and Ab-Initio Calculation of Magnetic Process in Orthorhombic YFe_xCr_(1-x)O₃ (0 ≤ x ≤ 1) Compounds. *Hyperfine Interact.* **2019**, *240*, 82. [[CrossRef](#)]
12. Popa, N.C. The (hkl) Dependence of Diffraction-Line Broadening Caused by Strain and Size for all Laue Groups in Rietveld Refinement. *J. Appl. Cryst.* **1998**, *31*, 176–180. [[CrossRef](#)]
13. Pecharsky, V.J.; Zavalij, P.Y. *Fundamentals of Powder Diffraction and Structural Characterization of Materials*, 2nd ed.; Springer Science Business Media, LLC: Berlin/Heidelberg, Germany, 2009; pp. 269–292, ISBN 978-0-387-09578-3.
14. Shi, L.R.; Xia, Z.C.; Wei, M.; Jin, Z.; Shang, C.; Huang, J.W.; Chen, B.R.; Ouyang, Z.W.; Huang, S.; Xiao, G.L. Unusual Effects of Ho³⁺ Ion on Magnetic Properties of YFe_{0.5}Cr_{0.5}O₃. *Ceram. Int.* **2015**, *41*, 13455–13460. [[CrossRef](#)]
15. Tiwari, B.; Surendra, M.K.; Rao, M.S.R. HoCrO₃ and YCrO₃: A Comparative Study. *J. Phys. Condens. Matter* **2013**, *25*, 216004. [[CrossRef](#)]
16. Shang, M.; Zhang, C.; Zhang, T.; Yuan, L.; Ge, L.; Yuan, H.; Feng, S. The Multiferroic Perovskite YFeO₃. *Appl. Phys. Lett.* **2013**, *102*, 062903. [[CrossRef](#)]
17. Mathur, S.; Veith, M.; Rapalaviciute, R.; Shen, H.; Goya, G.F.; Filho, W.L.M.; Berquo, T.S. Molecule Derived Synthesis of Nanocrystalline YFeO₃ and Investigations on Its Weak Ferromagnetic Behavior. *Chem. Mater.* **2004**, *16*, 1906–1913. [[CrossRef](#)]
18. Wu, L.; Yu, J.C.; Zhang, L.; Wang, X.; Li, S. Selective Self-Propagating Combustion Synthesis of Hexagonal and Orthorhombic Nanocrystalline Yttrium Iron Oxide. *J. Solid State Chem.* **2004**, *177*, 3666–3674. [[CrossRef](#)]
19. Cristóbal, A.A.; Botta, P.M.; Bercoff, P.G.; Ramos, C.P. Hyperfine and Magnetic Properties of a Y_xLa_{1-x}FeO₃ series (0 ≤ x ≤ 1). *Mater. Res. Bull.* **2015**, *64*, 347–354. [[CrossRef](#)]
20. Shen, J.; Xu, J.; Wu, A.; Zhao, J.; Shi, M. Magnetic and thermal properties of perovskite YFeO₃ single crystals. *Mater. Sci. Eng. B* **2009**, *157*, 77–80. [[CrossRef](#)]
21. Jacobs, I.S.; Burne, H.F.; Levinson, L.M. Field-Induced Spin Reorientation in YFeO₃ and YCrO₃. *J. Appl. Phys.* **1971**, *42*, 1631. [[CrossRef](#)]
22. Dahmani, A.; Taibi, M.; Noguez, M.; Aride, J.; Loudghiri, E.; Belayachi, A. Magnetic Properties of the Perovskite Compounds YFe_{1-x}Cr_xO₃ (0.5 ≤ x ≤ 1). *Mater. Chem. Phys.* **2003**, *77*, 912–917. [[CrossRef](#)]
23. Nair, V.; Das, A.; Subramanian, V.; Santhosh, P.N. Magnetic Structure and Magnetodielectric Effect of YFe_{0.5}Cr_{0.5}O₃. *J. Appl. Phys.* **2013**, *113*, 213907. [[CrossRef](#)]
24. Zhou, J.S.; Alonso, J.A.; Pomjakushin, V.; Goodenough, J.B.; Ren, Y.; Yan, J.Q.; Cheng, J.G. Intrinsic Structural Distortion and Superexchange Interaction in the Orthorhombic Rare-Earth Perovskites RCrO₃. *Phys. Rev. B* **2010**, *81*, 214115. [[CrossRef](#)]